

# Diode-laser absorption sensor for line-of-sight gas temperature distributions

Scott T. Sanders, Jian Wang, Jay B. Jeffries, and Ronald K. Hanson

Line-of-sight diode-laser absorption techniques have been extended to enable temperature measurements in nonuniform-property flows. The sensing strategy for such flows exploits the broad wavelength-scanning abilities ( $>1.7 \text{ nm} \approx 30 \text{ cm}^{-1}$ ) of a vertical cavity surface-emitting laser (VCSEL) to interrogate multiple absorption transitions along a single line of sight. To demonstrate the strategy, a VCSEL-based sensor for oxygen gas temperature distributions was developed. A VCSEL beam was directed through paths containing atmospheric-pressure air with known (and relatively simple) temperature distributions in the 200–700 K range. The VCSEL was scanned over ten transitions in the *R* branch of the oxygen *A* band near 760 nm and optionally over six transitions in the *P* branch. Temperature distribution information can be inferred from these scans because the line strength of each probed transition has a unique temperature dependence; the measurement accuracy and resolution depend on the details of this temperature dependence and on the total number of lines scanned. The performance of the sensing strategy can be optimized and predicted theoretically. Because the sensor exhibits a fast time response ( $\sim 30 \text{ ms}$ ) and can be adapted to probe a variety of species over a range of temperatures and pressures, it shows promise for industrial application. © 2001 Optical Society of America

*OCIS codes:* 300.1030, 300.6260, 280.3420, 140.2020, 120.1740, 120.6780.

## 1. Introduction

Nontomographic line-of-sight absorption sensors for gas temperature and species concentration traditionally have been limited to flows with near-uniform properties. However, because many flows of practical interest contain strong nonuniformities, several researchers have advanced strategies for nonuniform flows, particularly in the form of corrections for boundary layer effects.<sup>1,2</sup> More recently, a path-integrated sensor has been demonstrated for active control of a highly nonuniform flow,<sup>3,4</sup> a strategy for removing sensitivity to flow nonuniformities has been developed,<sup>5</sup> and an indicator for temperature nonuniformity along a line of sight has been suggested.<sup>6</sup>

Building on such previous research, in this paper we describe a novel strategy for extending line-of-sight temperature measurements to nonuniform

flows. The sensing strategy is enabled by recently developed vertical cavity surface-emitting laser (VCSEL) sources that provide rapid single-mode scans over a broad wavelength range ( $1.7 \text{ nm} \approx 30 \text{ cm}^{-1}$ ). Scanning approximately ten times farther than a traditional [Fabry–Perot or distributed feedback (DFB)] diode laser, a single VCSEL can probe many absorption transitions, yielding expanded temperature information. Although the temperature distributions inferred from this expanded information are not fully resolved, they are sufficient for many flow monitoring or control applications. Furthermore, VCSEL-based temperature distribution sensors offer the simplicity, affordability, and time response necessary for such applications.

Many practical systems contain significant nonuniformities in temperature and species concentration along candidate lines-of-sight for optical flow diagnostics. These nonuniformities are typically caused by heat transfer to surfaces, flow mixing, inhomogeneous combustion zones, buoyancy, and phase change. Temperature nonuniformities usually affect system performance, as processes such as chemical reaction, liquid evaporation, and material failure are all strongly temperature dependent. To optimize a flow for a given purpose, one often has to minimize, maximize, or in some way control the temperature gradients.

---

The authors are with the High Temperature Gasdynamics Laboratory, Department of Mechanical Engineering, Stanford University, Stanford, California 94305-3032. The e-mail address for S. T. Sanders is [ssanders@stanford.edu](mailto:ssanders@stanford.edu).

Received 2 January 2001; revised manuscript received 7 May 2001.

0003-6935/01/244404-12\$15.00/0

© 2001 Optical Society of America

The sensor described below interrogates multiple transitions in the (0–0) atmospheric A band of the molecular oxygen system  $O_2(b^1\Sigma_g^+) \leftarrow O_2(X^3\Sigma_g^-)$  to infer temperature distributions in the 200–700 K range; this approach is attractive because of the commercial availability of single-mode VCSELs near 760 nm and the ubiquity of oxygen. The portion of the  $O_2$  A band useful for temperature measurements in this range has been well characterized spectroscopically.<sup>7–9</sup> Other transitions in this system could be chosen to tailor future sensors to different temperature ranges.

Although several researchers have developed optical sensors for temperature based on  $O_2$  A-band transitions,<sup>10–13</sup> and others have used VCSELs to interrogate these transitions,<sup>14–16</sup> to the best of our knowledge no previous VCSEL absorption-based temperature sensors have been reported.

Oxygen is prevalent in the 200–700 K range in many flows where temperature uniformity is of great interest. For example, near the fuel injectors in a gas turbine engine, gas temperature and oxygen concentration govern fuel droplet evaporation and fuel–air mixture stoichiometry, which in turn affect engine performance. When gas property uniformities are maximized in this region, lower pollutant emissions and higher combustion efficiency can be realized.<sup>17,18</sup> Hence the sensor described here has potential for direct use in active control systems for (propulsion and stationary) gas turbines. Future sensors can employ identical techniques by use of different oxygen transitions (i.e., lines with different lower-state energies for different temperature ranges) or transitions of different species to obtain the information required by a specific application.

We begin by providing a theoretical basis for property distribution measurements in nonuniform flows. Two techniques for reducing absorption data to property distributions, the discretization technique and the distribution fitting technique, are described.

After providing this theoretical background, we demonstrate the sensor’s performance when applied to two atmospheric-pressure test cases with controlled nonuniformities: an air path composed of two segments, each with a different temperature, and an air path containing a linear temperature distribution. Although these test cases are common enough to represent potential sensor applications, the sensing strategy is not limited to these simple cases. A discussion of the sensor’s capabilities when applied to flows with more complex nonuniformities follows. Finally, discussions of line-shape fitting and absorption line selection, both applicable to nonuniform-path measurements, are presented.

## 2. Theory of Temperature Distribution Measurements

### A. Review of Uniform-Path Measurements

Along a uniform-property path, an absorber’s temperature and mole fraction have traditionally been measured by means of probing a pair of its absorption transitions.<sup>19,20</sup> This two-line technique has been

detailed previously.<sup>21</sup> In brief, the integrated absorbance areas  $a_1$  and  $a_2$  ( $\text{cm}^{-1}$ ) of the individual transitions, given by

$$a_i = \int_{-\infty}^{\infty} -\ln\left(\frac{I}{I_0}\right) d\nu, \quad (1)$$

are measured with a tunable, spectrally narrow source.  $I$  and  $I_0$  represent the transmitted and incident light intensities, respectively; and the integration is over frequency  $\nu$  ( $\text{cm}^{-1}$ ), implicitly taken to exclude all but the  $i$ th transition. Each area can be expressed as

$$a_1 = S_1(T)PxL, \quad a_2 = S_2(T)PxL, \quad (2)$$

where  $T$  (K) and  $x$  are the absorber temperature and mole fraction, respectively. The pressure of the probed volume  $P$  (atm) and the path length  $L$  (cm) are both usually known. The line strengths  $S_i$  ( $\text{cm}^{-2} \text{atm}^{-1}$ ) are given by

$$S_i(T) = S_i(T_0) \frac{Q(T_0)}{Q(T)} \left(\frac{T_0}{T}\right) \exp\left[-\frac{hcE_i''}{k} \left(\frac{1}{T} - \frac{1}{T_0}\right)\right] \times \left[1 - \exp\left(\frac{-hc\nu_{0,i}}{kT}\right)\right] \left[1 - \exp\left(\frac{-hc\nu_{0,i}}{kT_0}\right)\right]^{-1}, \quad (3)$$

where  $T_0$  (K) is a reference temperature;  $Q$  is the absorber’s partition function; and  $\nu_{0,i}$  ( $\text{cm}^{-1}$ ) and  $E_i''$  ( $\text{cm}^{-1}$ ) are the frequency and lower-state energy of the  $i$ th transition, respectively.

The ratio of the areas  $a_1/a_2$  thus can be reduced to a function only of the absorber temperature  $T$ :

$$R \equiv \frac{a_1}{a_2} = f(T) \approx \frac{S_1(T_0)}{S_2(T_0)} \times \exp\left[-\left(\frac{hc}{k}\right)(E_1'' - E_2'')\left(\frac{1}{T} - \frac{1}{T_0}\right)\right]. \quad (4)$$

Using the measured areas  $a_1$  and  $a_2$ , researchers typically solve Eqs. (2) for the two unknowns,  $T$  and  $x$ , by finding  $T$  with Eq. (4) and  $x$  with one of Eqs. (2).

### B. Discretization Technique

When the path of interest contains nonuniformities, additional lines, each with a unique temperature dependence, can be probed to determine an approximate temperature distribution along the path. As shown above, two area measurements yielded two flow parameters,  $T$  and  $x$ ; three area measurements could be used to obtain three flow parameters, for example,  $T_1$ ,  $T_2$ ,  $x$ , and so on. For the general problem, we can model the nonuniform-property path as being composed of  $n$  nearly uniform property path segments, each with a temperature  $T_i$ , pressure  $P_i$ , mole fraction  $x_i$ , and path length  $L_i$ . Denoting the

product of the last three quantities as  $(PxL)_i$ , we can generalize Eq. (2) as

$$\begin{bmatrix} S_1(T_1) & S_1(T_2) & \cdots & S_1(T_n) \\ S_2(T_1) & S_2(T_2) & \cdots & S_2(T_n) \\ \vdots & \vdots & \ddots & \vdots \\ S_m(T_1) & S_m(T_2) & \cdots & S_m(T_n) \end{bmatrix} \begin{bmatrix} (PxL)_1 \\ (PxL)_2 \\ \vdots \\ (PxL)_n \end{bmatrix} = \begin{bmatrix} a_1 \\ a_2 \\ \vdots \\ a_m \end{bmatrix}, \quad (5)$$

or

$$\mathbf{S}\mathbf{x} = \mathbf{a},$$

where  $m$  is the number of absorption lines probed in the measurement of the vector of integrated absorbance areas  $\mathbf{a}$ . If the possible temperatures  $(T_1, T_2, \dots, T_n)$  in the path are postulated and the spectroscopic parameters in Eq. (3) are known, then the matrix  $\mathbf{S}$  is known and the solution  $\mathbf{x}$  can be found. Because each element of  $\mathbf{x}$  must be positive, it is usually best to use a nonnegative least-squares (NNLS) algorithm to solve Eq. (5). Typically, the pressure  $P$  is uniform and known and therefore can be divided out of the vector  $\mathbf{x}$ , leaving the solution  $[(xL)_1, (xL)_2, \dots, (xL)_n]^T$ . The product  $xL$  is termed the column density; in general, the discretization technique determines the column density present in each specified temperature bin defined by the postulated temperatures  $(T_1, T_2, \dots, T_n)$ . No information regarding the way in which the constituent column densities are arranged along the path is obtained.

Depending on simplifications allowed by a specific application, the column density solution vector can be reduced to more meaningful information. For example, if the absorber mole fraction is known to be uniform, the mole fraction can be determined and divided out, leaving the vector  $(L_1, L_2, \dots, L_n)^T$ . This vector can be divided by the total path length,  $L_1 + L_2 + \dots + L_n$ , to yield the fraction of gas assigned to each temperature bin. Such simplifications are detailed below in Section 3.

The error in the solution vector  $\mathbf{x}$  is governed by the condition number of  $\mathbf{S}$ , which in turn depends on the number of absorption transitions probed  $m$ , the spectroscopic properties of the absorption transitions (particularly the lower-state energies  $E_i''$ ), and the number of temperature bins  $n$ . For example, if many temperature bins are used,  $\text{cond}(\mathbf{S})$  is large, and therefore the measurement error is relatively high. The condition number, and its utility for choosing absorption lines for temperature distribution measurements, is detailed below in Subsection 4.C.

### C. Distribution Fitting Technique

The discretization technique has two main advantages: It is fast because a linear system is solved, and it requires little *a priori* knowledge of the temperature distribution in the flow [i.e., if a temperature bin vector  $(T_1, T_2, \dots, T_n)$  is chosen with equally spaced bins, only the expected minimum and maxi-

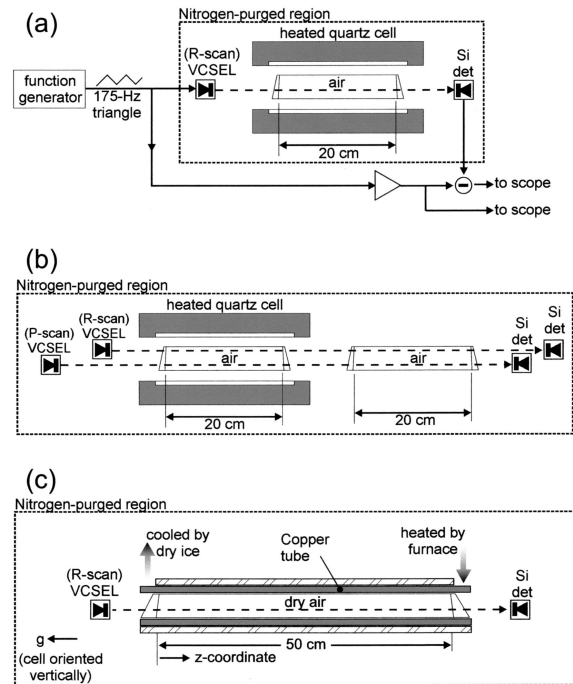


Fig. 1. Demonstration experiments: sensor applied to (a) uniform-temperature path measurement, (b) two-temperature path measurement employing two lasers, and (c) path containing a linear temperature distribution. Note that in case (c) the cell is oriented vertically to stratify the air, providing a stable temperature distribution.

imum temperatures,  $T_1$  and  $T_n$ , are required]. Its major drawback is that the discretization may be too coarse unless many bins are used, and too many bins can result in an ill-conditioned problem. Therefore it is often advantageous for one to assume a general form for the temperature and mole fraction distributions in the flow and obtain the best-fit distributions for a given measurement of the area vector  $\mathbf{a}$  using a nonlinear function minimization algorithm. Use of this technique requires that a suitable form for the distributions can be assumed. Because the assumption of such a functional form effectively constrains the problem, the distribution fitting technique is typically more stable than the discretization technique.

The same area data  $\mathbf{a}$  can be analyzed with either technique, as is demonstrated in Section 3. The resolution and accuracy of either technique increase with the number of lines scanned, especially if lines with appropriate lower-state energies are chosen (see Section 4).

## 3. Demonstration Experiments

### A. Sensor Description

A temperature distribution sensor was demonstrated for three controlled test cases: a uniform-temperature path [Fig. 1(a)], a path containing two temperatures [Fig. 1(b)], and a path with a linear temperature distribution [Fig. 1(c); in this case the cell is oriented vertically to stratify the gas]. Type S thermocouples are used in all cases to determine the

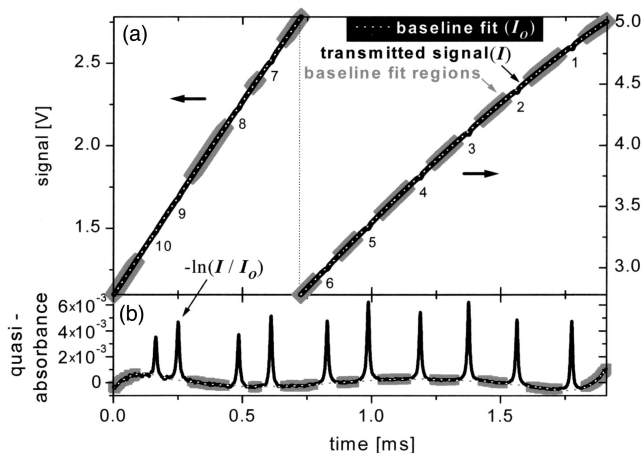


Fig. 2. Raw data trace highlighting baseline fitting routines. Lines are numbered and can be referenced in Table 1.

actual air temperatures. The VCSEL (CSEM760, Centre Suisse d'Electronique et de Microtechnique, Switzerland) is held at a constant case temperature while triangle current modulation (175 Hz) is applied. An off-axis parabolic mirror ( $f = 1$  cm, not shown) collimates the VCSEL light, forming a 3-mm-diameter beam. The VCSEL beam is directed through the (case-specific) atmospheric-pressure air path, and the transmitted intensity is monitored by a silicon detector. The VCSEL, air path, and detector are enclosed in a nitrogen-purged environment to remove room  $O_2$  interference.

To reduce bit noise, the (amplified) function generator signal is subtracted from the detector signal before digitization on a 12-bit, 5-megasamples/s scope. The function generator signal is also digi-

tized, and the two digital signals are then added to reconstruct the (essentially bit-noise-free) transmitted intensity signal. A sample transmitted signal [corresponding to the 292 K data of Fig. 3(b)] is shown in Fig. 2(a). This signal, corresponding to the transmitted intensity  $I$  of Eq. (1), contains ten absorption lines. A fixed number of data points about each line center is deleted from the transmitted signal in Fig. 2(a), leaving the segmented trace labeled baseline fit regions. A third-order polynomial is fit to this trace and is called the baseline fit. The baseline fit approximates  $I_0$  in Eq. (1). An initial determination of absorbance, termed quasi-absorbance because the value of  $I_0$  is imperfect, is then calculated as  $-\ln(I/I_0)$ ; see Fig. 2(b). A second polynomial is then fit to the baseline fit regions in Fig. 2(b) and subtracted from the quasi-absorbance trace; the result is the (true) absorbance, shown in all subsequent spectra in this paper containing measured spectra. Each measured spectrum has a minimum detectable absorbance of  $\sim 1 \times 10^{-4}$ . The known line positions, listed in Table 1, are used to convert the time axis to absolute optical frequency.

The data shown in Fig. 2(a) are an average of 16 consecutive traces, each digitally filtered to 150 kHz (as are the traces in all subsequent figures); thus the time required to record the data for each temperature distribution measurement presented is  $16 \times 1.9$  ms  $\approx$  30 ms. The minimum detectable absorbance of  $1 \times 10^{-4}$  is essentially the lower limit for these conditions based on the relative intensity noise of the lasers.<sup>14</sup> If the technique is applied for stronger absorbers or over a longer path length (eliminating the need for averaging), the temperature distribution measure-

Table 1. Spectroscopic Data Used in the Computations

Line Number (this paper)	Positions <sup>a</sup> (cm <sup>-1</sup> )	$S(296) \times 10^{5b}$ (cm <sup>-2</sup> atm <sup>-1</sup> )	$S(296 \times 10^{5a})$ (cm <sup>-2</sup> atm <sup>-1</sup> )	$E''^a$ (cm <sup>-1</sup> )	Assignment <sup>a</sup> ( $\Delta NN \Delta JJ$ )	
<i>R</i> Scan						
1	13138.19389	20.07	19.95	42.224	<i>R</i> 5	<i>Q</i> 6
2	13140.55687	18.33	18.27	81.581	<i>R</i> 7	<i>R</i> 7
3	13142.57276	21.99	21.89	79.565	<i>R</i> 7	<i>Q</i> 8
4	13144.53073	18.62	18.51	130.44	<i>R</i> 9	<i>R</i> 9
5	13146.57050	21.53	21.41	128.40	<i>R</i> 9	<i>Q</i> 10
6	13148.12585	16.96	16.86	190.77	<i>R</i> 11	<i>R</i> 11
7	13150.18729	19.11	19.06	188.71	<i>R</i> 11	<i>Q</i> 12
8	13151.34015	14.13	14.05	262.58	<i>R</i> 13	<i>R</i> 13
9	13153.42196	15.62	15.62	260.50	<i>R</i> 13	<i>Q</i> 14
10	13154.17134	10.80	10.81	345.85	<i>R</i> 15	<i>R</i> 15
<i>P</i> Scan						
11	13033.19673	1.895	1.910	791.40	<i>P</i> 23	<i>Q</i> 22
12	13031.39115	1.960	2.004	793.21	<i>P</i> 23	<i>P</i> 23
13	13023.07776	—	1.053	931.74	<i>P</i> 25	<i>Q</i> 24
14	13021.29000	—	1.099	933.53	<i>P</i> 25	<i>P</i> 25
15	13012.58414	—	0.545	1083.4	<i>P</i> 27	<i>Q</i> 26
16	13010.81402	—	0.567	1085.2	<i>P</i> 27	<i>P</i> 27

<sup>a</sup>From the HITRAN database.<sup>9</sup>

<sup>b</sup>From Brown and Plymate.<sup>7</sup>

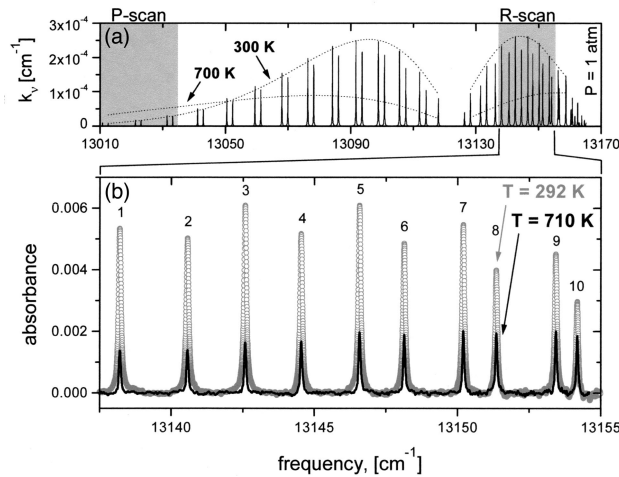


Fig. 3. (a) HITRAN prediction of O<sub>2</sub> A-band absorption, showing the R-scan and P-scan regions probed. (b) Data recorded in two uniform-temperature path experiments ( $P = 1$  atm,  $L = 20$  cm) at temperatures of 292 and 710 K.

ments can be made very rapidly because both the VCSEL scan range and the scan rate are greatly enhanced over DFB lasers.<sup>14</sup> We observed scan rates of up to  $6 \text{ cm}^{-1} \mu\text{s}$  with the VCSELs used in these demonstrations; this scan rate enables a temperature distribution measurement time of  $5 \mu\text{s}$  if a  $30\text{-cm}^{-1}$  scan range is required.

Figure 3(a) shows a theoretical O<sub>2</sub> A-band spectrum calculated from HITRAN.<sup>9</sup> The two VCSEL scan ranges used in these demonstration experiments, labeled R scan and P scan, are highlighted in the figure. The spectroscopic data for the lines probed by the scans are listed in Table 1, numbered 1–16 for clarity [two  $S(296)$  data columns are presented in Table 1; we used the recent data of Brown and Plymate<sup>7</sup> for our computations except for measurements involving the P-scan lines; Ref. 7 data are unavailable for P-scan lines, therefore we used the HITRAN<sup>9</sup> data. The R-scan lines were chosen for their spectral proximity, allowing ten lines to be encompassed by a single VCSEL scan. These lines are often adequate for O<sub>2</sub> temperature distribution measurements in the 200–700 K range. Although sensitivity would be improved if we expanded the R scan to the right on Fig. 3(a), encompassing lines with higher  $E''$  values, the complexities of the bandhead discourage this, at least for the present demonstration experiments. Instead, to improve temperature sensitivity, especially above  $\sim 500$  K, the P-scan lines are added. The P-scan lines have higher  $E''$  values than the R-scan lines and thus improve the condition number of the line-strength matrix  $\mathbf{S}$  and the measurement uncertainty, as explained in Section 4.

#### B. Uniform Temperature Path: R Scan Only

Although the temperature distribution sensor is not required for uniform flows, we discuss its application to a uniform-temperature test case here for complete-

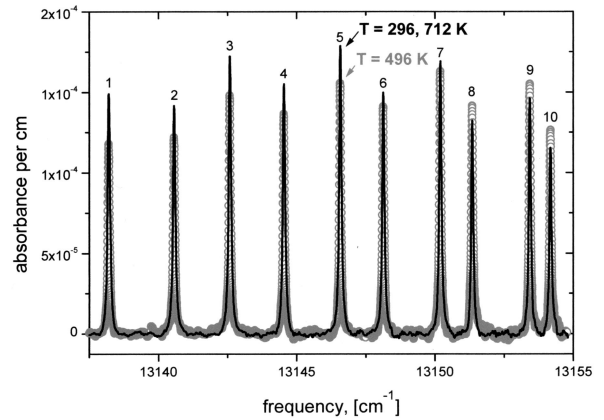


Fig. 4. Comparison of absorbance data recorded in a uniform-temperature path (496 K,  $L = 20$  cm) with data recorded in a two-temperature (296 K,  $L = 20$  cm; in series with 712 K,  $L = 20$  cm) path, each divided by the total path length. Although 496 K is nearly the mean of 296 and 712 K, the traces are easily distinguishable, graphically demonstrating the plausibility of the temperature distribution sensing strategy.

ness. As shown in Fig. 1(a), the VCSEL beam is directed through a quartz cell (20-cm path length) containing air at a known uniform (to within 3%) temperature. The laser is tuned over the R-scan lines of the O<sub>2</sub> A band, and the data recorded in two different uniform-temperature experiments ( $T = 292$  K, 710 K) are shown in Fig. 3(b). Figure 4 shows data for  $T = 496$  K (open circles) taken in the same configuration, but plotted as absorbance per centimeter to facilitate a future comparison. We determined the areas of each line scanned for the three uniform-temperature cases ( $T = 292$  K, 496 K, 710 K) using Voigt fits, which yielded the following three  $\mathbf{a}$  vectors:

$$\begin{aligned}
 \mathbf{a}_{292} &= \begin{bmatrix} 8.70 \times 10^{-4} \\ 8.08 \times 10^{-4} \\ 9.67 \times 10^{-4} \\ 7.99 \times 10^{-4} \\ 9.45 \times 10^{-4} \\ 7.27 \times 10^{-4} \\ 8.35 \times 10^{-4} \\ 6.08 \times 10^{-4} \\ 6.78 \times 10^{-4} \\ 4.48 \times 10^{-4} \end{bmatrix} & \mathbf{a}_{496} &= \begin{bmatrix} 3.18 \times 10^{-4} \\ 3.18 \times 10^{-4} \\ 3.85 \times 10^{-4} \\ 3.59 \times 10^{-4} \\ 3.88 \times 10^{-4} \\ 3.60 \times 10^{-4} \\ 4.17 \times 10^{-4} \\ 3.54 \times 10^{-4} \\ 3.61 \times 10^{-4} \\ 3.02 \times 10^{-4} \end{bmatrix} \\
 \mathbf{a}_{710} &= \begin{bmatrix} 1.64 \times 10^{-4} \\ 1.71 \times 10^{-4} \\ 1.89 \times 10^{-4} \\ 2.13 \times 10^{-4} \\ 2.30 \times 10^{-4} \\ 2.11 \times 10^{-4} \\ 2.20 \times 10^{-4} \\ 2.28 \times 10^{-4} \\ 2.15 \times 10^{-4} \\ 2.13 \times 10^{-4} \end{bmatrix} & & (\text{cm}^{-1}).
 \end{aligned}$$

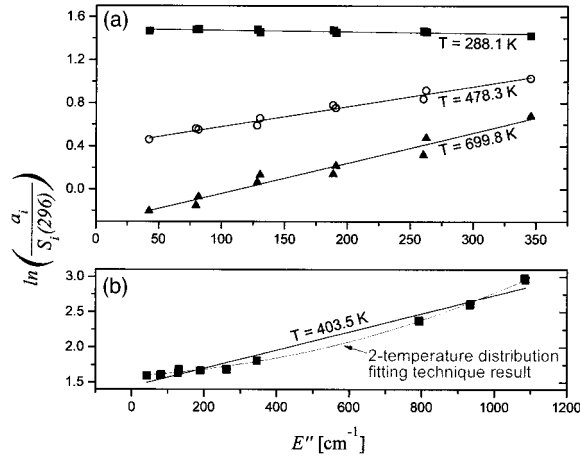


Fig. 5. Boltzmann plots for (a) uniform-temperature path measurements ( $T_{\text{actual}} = 292, 496,$  and  $710 \text{ K}$ ) with  $R$  scan only and (b) two-temperature path measurement ( $T_{\text{actual}} = 296, 712 \text{ K}$ ) with both  $R$  and  $P$  scans. Temperature labels correspond to best-fit lines through the measurements.

The first component of each vector is the area of line 1, and the last is the area of line 10.

Before applying the discretization and distribution fitting techniques to these data, we present a standard technique for determining temperature: the Boltzmann plot of Fig. 5(a). The best-fit lines through the data provide the measured temperatures of 288.1, 478.3, and 699.8 K, which are within 1.3%, 3.6%, and 1.4%, respectively, of the actual gas temperatures. Figure 5(a) shows the measurement error (scatter about the best-fit lines) increasing with temperature, which is due to the reduced absorbance as shown in Fig. 3(b).

The standard Boltzmann plot is not an appropriate means for determining temperature in nonuniform flows. Figure 5(b) shows a Boltzmann plot for measurements (presented below in Fig. 7) from the two-temperature path configuration [Fig. 1(b)]. The temperature nonuniformity causes significant curvature in the data; the actual cell temperatures are 296 and 712 K, but the best-fit line determines an intermediate temperature of 403.5 K. Both the discretization and the distribution fitting techniques, when applied to nonuniform-temperature flows, yield results that exhibit the necessary curvature on the Boltzmann plot.

To apply the discretization technique to the above area vectors  $\mathbf{a}$ , we first generate a  $10$  (lines)  $\times$   $7$  (equally spaced  $T$  bins) matrix  $\mathbf{S}$  with  $T_1 = 200 \text{ K}$  and  $T_7 = 800 \text{ K}$  using the data of Table 1 (Brown and Plymate line-strength data). Using the three measured  $\mathbf{a}$  vectors, we then solve Eq. (5) three times for  $\mathbf{x}$  using a NNLS algorithm. The  $\mathbf{x}$  vectors are divided by the known pressure of 1 atm to obtain the column density in each specified temperature bin; these results are shown in histogram form in Fig. 6. In this simple case, we can also divide by the known path length of 20 cm to obtain the mole fraction of  $\text{O}_2$  in each temperature bin, also shown in Fig. 6.

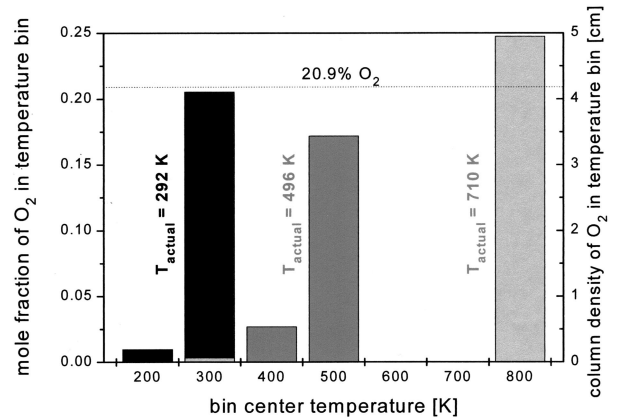


Fig. 6. Results of uniform-temperature path measurements with the discretization technique. Because none of the temperatures probed are exactly the bin center temperatures, a compromise between two bins is obtained in all cases. Bars corresponding to the actual conditions would be centered at the  $T_{\text{actual}}$  and have a height of 0.209.

Figure 6 demonstrates that, with only the  $R$  scan active, the sensor performs best at relatively low temperatures. This trend is partly because the condition number of  $\mathbf{S}$  increases with temperature (see Subsection 4.C) and partly because the error in  $\mathbf{a}$  increases with temperature [as shown in Fig. 5(a)]. The 292 K result is nearly perfect: The ideal result would be a bar of height 0.209 at  $T = 292 \text{ K}$ , but the discretization forces a compromise between the bins at 200 and 300 K. The results for the higher-temperature tests could be improved if we probed additional lines such as the  $P$ -scan lines.

Of course, because the path temperature is known to be uniform in this case, the binwise results of the discretization technique shown in Fig. 6 are not as meaningful as a single temperature and mole fraction. As we illustrate below, the discretization technique is most useful for providing a snapshot of a path's temperature content, particularly when little is known about the path *a priori*.

The distribution fitting technique can be applied to the same three  $\mathbf{a}$  vectors. For this simple case, the distribution fitting technique amounts to our finding the single temperature and  $\text{O}_2$  mole fraction that best replicate each measured  $\mathbf{a}$  vector. This problem is much more constrained than the discretization problem, and the results are good for all three temperatures: The measured temperatures are 290, 479, and 695 K and are within 0.7%, 3.4%, and 2.4%, respectively, of the actual values and in good agreement with the values obtained from Fig. 5(a). The measured mole fractions are 0.212, 0.196, and 0.208 and are within 1.4%, 6.2%, and 0.5%, respectively, of the actual value 0.209.

### C. Two-Temperature Path: $R$ Scan Only

In the second configuration [Fig. 1(b)], the VCSEL beam is directed through two quartz cells in series (each with a 20-cm path length) containing room air

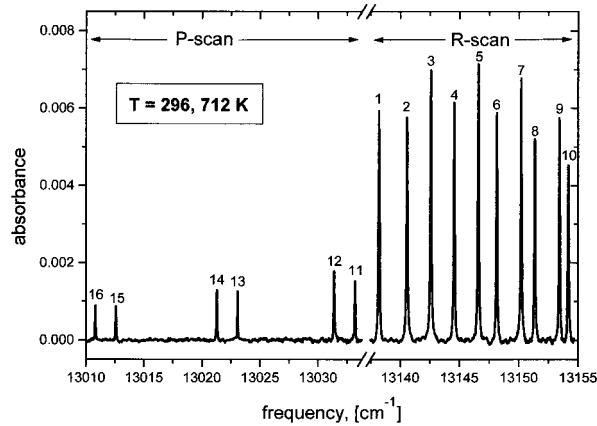


Fig. 7. Data recorded in a two-temperature (296, 712 K) path measurements with both the *R*-scan and the *P*-scan VCSELs.

at temperatures of 712 and 296 K, respectively. The *R*-scan lines are probed, and the resulting absorbance data are divided by the total path length of 40 cm to obtain the absorbance per centimeter data shown as a solid curve in Fig. 4. The open circles in Fig. 4 are the data recorded in the 496 K uniform-temperature path. Because the columns of **S** are linearly independent, the two traces in Fig. 4 are easily distinguished, even though 496 K is approximately the mean of 296 and 712 K. Graphically, this is why temperature distribution measurements are possible. The lower the condition number of **S**, the less data such as those compared in Fig. 4 will look alike and the lower the temperature distribution measurement errors will be (see Subsection 4.C).

To measure the temperature distribution in the two-temperature path, we first determine the area vector **a** from the data of Fig. 4 using the hybrid line-shape fitting method (described in Section 4). The discretization and the distribution fitting techniques can now be applied. However, with only the *R* scan active, the results of the discretization technique are extremely sensitive to the temperature bin vector, and therefore they are not reported here. As demonstrated in Subsection 3.D, the addition of the *P*-scan lines improves the condition of **S** and enables stable discretization technique results for this two-temperature path. Because it is able to impose more constraints, the distribution fitting technique outperforms the discretization technique when only the *R* scan is active. Specifying that the 40-cm path is really composed of two uniform-property paths, each 20 cm long, and *x* is uniform throughout, we can use the distribution fitting technique to determine which two temperatures and single mole fraction (three parameters) best reproduce the measured data. The results are  $T_1 = 293$  K,  $T_2 = 768$  K, and  $x_{O_2} = 0.209$ , which are within 1.4%, 7.8%, and 0.0%, respectively, of the actual values.

#### D. Two-Temperature Path: *R* Scan Plus *P* Scan

To enhance the results of both techniques, we add a second VCSEL [shown in Fig. 1(b)] to the setup and

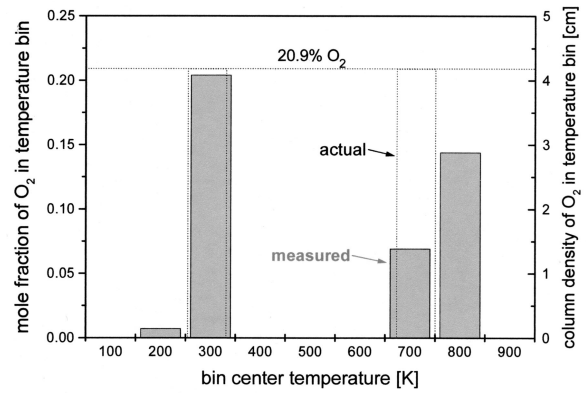


Fig. 8. Results of two-temperature path measurements with the discretization technique. Dashed bars correspond to actual conditions and cannot be matched exactly by the sensor because the bin center temperatures are fixed.

additionally probe the *P*-scan lines (the additional VCSEL beam could be time-division or phase-division multiplexed if both beams were required to probe the same path). With the cells still maintained at 712 and 296 K, the data shown in Fig. 7 are acquired, from which the **a** vector is determined. Because we changed *m* by adding the *P*-scan lines, a new matrix **S** must now be formed: A 16 (lines)  $\times$  9 (equally spaced *T* bins) matrix **S** with  $T_1 = 100$  K and  $T_7 = 900$  K is generated by use of the data of Table 1 (HITRAN line-strength data). This time the discretization method yields an acceptable solution vector **x**, shown in Fig. 8. The vertical scale on the right shows **x** divided by the known pressure of 1 atm to obtain column density. On the left, **x** is divided by the cell path length of 20 cm for comparison with Fig. 6. Note that the actual path conditions, plotted for comparison in Fig. 8, could be obtained by the sensor only if the bin center temperatures were allowed to vary.

Figure 8 highlights the sensor's potential for use in engineering applications: The sensor can provide rapid temperature distribution information (every 30 ms in this case) of the type shown. Whereas previous sensors that use Fabry–Perot or DFB lasers have been limited to providing a single temperature and mole fraction along a line of sight, the VCSELs used by this sensor effectively allow a range of temperatures and mole fractions to be measured. To illustrate the utility of such expanded information, let us consider applying the sensor to monitor flow properties near the fuel injectors in a gas turbine engine. Typically, maximum uniformity (i.e., all the  $O_2$  in a single temperature bin rather than distributed as in Fig. 8) is desired in this region.<sup>17,18</sup> If the major temperature components in the flow are measured, the sensor could reveal unwanted hot spots, cold spots, and exceptionally broad temperature distributions. In general, the sensor's ability to rapidly report data of the type shown in Fig. 8 should be useful for controlling any system that is affected by significant changes in its temperature distributions.

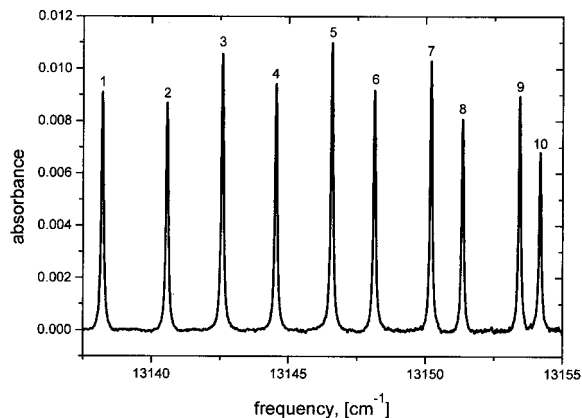


Fig. 9. Data recorded in a linear temperature distribution measurement.

With both the *R*-scan and *P*-scan VCSELs active, we can apply the distribution fitting technique again using known system information. This time we specify only that the measured system be composed of two uniform-property paths, each 20 cm long, which relaxes a constraint from the three-parameter fit performed above because it allows nonuniform mole fraction  $x$ . The two temperatures and two mole fractions (four parameters) that best fit the data are determined to be  $T_1 = 284$  K,  $T_2 = 687$  K,  $x_{O_2,1} = 0.188$ , and  $x_{O_2,2} = 0.225$ . These best-fit temperatures and mole fractions are within 4% and 10%, respectively, of the actual values. It is interesting to note that, if we use the traditional two-line technique (employing lines 2 and 12 as a representative test case) to measure the temperature and mole fraction along this path, we find  $T = 380$  K and  $x_{O_2} = 0.189$ .

We successfully conditioned the line-strength matrix  $\mathbf{S}$  to higher temperatures by adding the *P*-scan lines, improving the results of both data reduction techniques. Attempts to add even higher-energy *P*-branch lines (better conditioning  $\mathbf{S}$  for combustion temperatures, for example) will meet two challenges. First, the line strengths will be lower than those used in the present experiments. Lower line strengths could demand use of more sensitive wavelength modulation spectroscopy techniques,<sup>14</sup> depending on the available path length. Second, room-temperature line strengths  $S_i(296)$  will be less well known; the precise data of Brown and Plymate terminate at the *P*23–*P*23 line as shown in Table 1, and the HITRAN data become increasingly suspect above this point. Further fundamental studies of the room-temperature line strengths  $S_i(296)$  of the higher-energy lines may therefore be required.

#### E. Linear Temperature Distribution: *R* Scan Only

In the third configuration [Fig. 1(c)], the VCSEL beam is directed through a 50-cm-long cell containing atmospheric-pressure dry air (Praxair extra-dry grade) with a linear temperature distribution ranging from 230 to 620 K. The cell is housed in a vertical copper tube that ensures this distribution: The

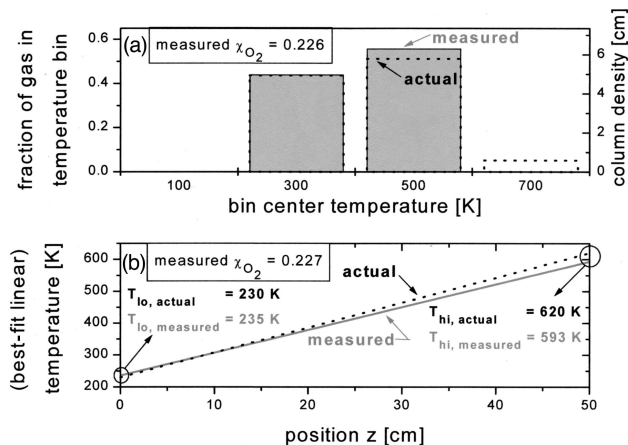


Fig. 10. (a) Discretization technique and (b) distribution fitting technique results from a linear temperature distribution measurement. The measured linear temperature distribution (b) is everywhere within 5% of the actual linear temperature distribution.

bottom end of the copper tube is cooled by dry ice, and the top end is heated by a furnace.

A sample absorbance trace, obtained by probing the *R*-scan absorption lines, is shown in Fig. 9. Because of the slightly longer path length and the cooler temperature portion, the peak absorbances are greater than in previous figures, resulting in a higher signal-to-noise ratio. The  $\mathbf{a}$  vector obtained from Fig. 9 is therefore very close (within 1.4%) to the theoretical  $\mathbf{a}$  vector for this case. Therefore, even though only the *R*-scan lines are probed, the discretization technique yields good results if relatively few temperature bins are used. After generating a  $10$  (lines)  $\times$   $4$  (equally spaced  $T$  bins) matrix  $\mathbf{S}$  with  $T_1 = 100$  K and  $T_4 = 700$  K using the data of Table 1 (Brown and Plymate line-strength data), we obtained the solution vector  $\mathbf{x}$  using a NNLS algorithm. We found the column density, shown in Fig. 10(a) (right vertical axis), by dividing  $\mathbf{x}$  by the known pressure of 1 atm. To determine the total  $O_2$  mole fraction, the vector  $\mathbf{x}$  is divided by the known pressure of 1 atm and the known total path length of 50 cm, and the result is termed  $\mathbf{x}'$ . The sum of the elements of  $\mathbf{x}'$  is the measured value of  $x_{O_2}$ , 0.226 in this case. The vector  $\mathbf{x}''$ , formed by dividing  $\mathbf{x}'$  by  $x_{O_2}$ , represents the fraction of absorber in each temperature bin;  $\mathbf{x}''$  is plotted in Fig. 10(a) on the left vertical axis. The measured data shown in Fig. 10(a) are compared with the actual binwise discretization of the known linear temperature distribution. Because of the reduced number of bins employed, the discretization is relatively coarse, but the agreement between the measured and the actual discretizations demonstrates the sensor's fidelity. Even when coarsely discretized, the sensor is potentially useful for applications requiring a broad sense of the temperature nonuniformity.

When the distribution fitting technique is used to interpret the same  $\mathbf{a}$  vector, the best-fit uniform-mole-fraction linear temperature distribution is

found to have  $T_{lo} = 235$  K,  $T_{hi} = 593$  K, and  $x_{O_2} = 0.227$ . This result is plotted in Fig. 10(b). The measured temperature distribution is everywhere within 5% of the actual (thermocouple-verified) distribution. By imposing the known form for the temperature distribution, we made the same data that generated the coarse discretization of Fig. 10(a) to generate the more meaningful results of Fig. 10(b).

The above experiments demonstrate that, in flows containing simple nonuniformities, the distribution fitting technique is more robust than the discretization technique because it incorporates additional (user-supplied) information. The distribution fitting technique is especially useful whenever a simple and accurate functional form for the property distributions in the flow is known or can be assumed. When such a form is not available (i.e., in the case of unknown or complex flow properties), the discretization technique may be favorable; this is especially true if approximate information is sufficient (i.e., if one is looking only for the appearance of a cold zone in a hot system) or if computational cost must be minimized (i.e., for rapid control applications).

#### 4. Discussion

##### A. Complex Nonuniformities in Temperature and Mole Fraction

The demonstration experiments described above had uniform mole fraction  $x$ . However, in Subsection 3.D, the distribution fitting problem was easily cast to allow mole fraction nonuniformity. The distribution fitting technique is especially useful whenever coincident mole fraction and temperature nonuniformities are expected along a path of interest. The discretization technique can still be applied, and, as always, it provides the column density present in each temperature bin. However, the column density information becomes less meaningful as the mole fraction nonuniformity becomes more severe (i.e., a hot spot containing a low mole fraction of the absorber may go undetected because its contribution to column density is small). The distribution fitting technique can provide more meaningful results, especially if the local mole fraction can be expressed as a single-valued function of local flow temperature. For example, in a reacting flow with heat transfer to walls, one might specify a parabolic distribution for temperature and also prescribe  $x_{\text{absorber}} = c \times f(T)$  everywhere along the probe path, where  $c$  is a parameter determined in the fit and  $f$  might return the equilibrium mole fraction of the probed species at temperature  $T$ . Similar prescriptions could be made in cases in which the probed path interrogates the mixing of two flows. If the local temperature and mole fraction are statistically dependent, and if intelligent (application-specific) distribution functionalities can be assumed, the distribution fitting problem can provide meaningful results even for flows with somewhat complex nonuniformities. In flows with exceptionally complex nonuniformities, or when spatial information is required, it may be useful

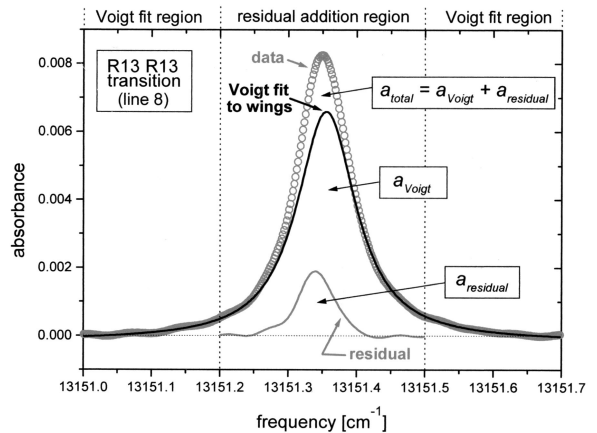


Fig. 11. Hybrid line-shape fitting method used to determine the area of line shapes recorded in nonuniform-temperature paths.

to combine the techniques of this paper with existing tomographic techniques.<sup>22</sup>

##### B. Hybrid Line-Shape Fitting for Nonuniform-Temperature Paths

For the uniform-temperature path measurements described in Subsection 3.B, the determination of the  $\mathbf{a}$  vector from the data (i.e., from Fig. 2) was straightforward. With isolated lines and a single temperature, standard baseline and Voigt fitting routines provided accurate integrated absorbance areas  $a_i$ . It is important to note that no line-shape broadening information was input to the fitting routine used to determine the areas  $a_i$ ; this is a great advantage because the broadening parameter  $2\gamma(T, P, x_j)$  is usually unknown.

Complications arise when  $\mathbf{a}$  must be determined in flows with nonuniform temperatures. To our knowledge, few if any previous publications have discussed these complications or attempted to determine accurate line-shape areas in highly nonuniform flows. Here we discuss the complications, including the additional challenges caused by high pressures, and offer a hybrid line-shape fitting method as a solution to determining  $\mathbf{a}$  in nonuniform flows.

Consider first the two-temperature case of Fig. 1(b). If the two temperatures are considerably different, each line shape recorded will be poorly modeled by a single Voigt profile. The proper profile would be a sum of two Voigt functions with different collisional widths, different Doppler widths, and different line-center positions. Such a fit could be performed, but if we move to a continuously varying temperature distribution such as the linear distribution of Fig. 1(c), this approach becomes unreliable unless  $2\gamma(T, P, x_j)$  is known. Even if  $2\gamma(T, P, x_j)$  is known, the approach is computationally costly. Rather than attempting such complicated fitting procedures, we could numerically integrate the data as suggested by Eq. (1). This approach, however, generally provides systematically low estimates of  $a_i$  be-

cause the line-shape area contained in the far wings, where the signal-to-noise ratio is  $<1$ , is sacrificed.

To solve this problem, we adopted the hybrid line-shape fitting method depicted in Fig. 11. The feature shown in Fig. 11 is a closeup of the R13–R13 transition from the linear temperature distribution data shown in Fig. 9. The hybrid fitting method is performed as follows. The central  $0.3\text{ cm}^{-1}$  of the data is temporarily ignored, and a Voigt fit is applied to the remaining wings, fixing the Doppler width at the appropriate value for the (application-specific) lowest expected temperature (200 K in this case). This resulting fit area is called  $a_{\text{Voigt}}$ . The fit curve is then subtracted from the original data, yielding the residual. The residual is integrated numerically over the central  $0.3\text{ cm}^{-1}$ , and the result  $a_{\text{residual}}$  is added to  $a_{\text{Voigt}}$  to obtain the desired line-shape area  $a_{\text{total}}$ . This hybrid method works because the fit to the Voigt wings maintains the baseline accuracy sacrificed by numerical integration whereas the numerical integration handles the complicated behavior near the line center where the signal-to-noise ratio is high. The method is used to find all areas  $a_i$  in the nonuniform-temperature experiments described in this paper. The method was found to perform well and remains independent of *a priori* knowledge of  $2\gamma(T, P, x_j)$ . Depending on the line-shape broadening in a specific application, a Lorentzian or Doppler fit can in many cases be substituted for the Voigt fit to enhance the speed of the hybrid fitting method.

The hybrid fitting method can be used in nonuniform flows to arbitrarily high pressures, as long as the baseline fitting technique shown in Fig. 2 is not compromised. For  $\text{O}_2$  A-band transitions in the *P* branch, this condition limits the technique to approximately 10 atm at room temperature and 30–40 atm at combustion temperatures. However, when spectrally dense features (common in polyatomic species or near the bandhead in the A-band *R* branch of  $\text{O}_2$ ) must be probed, blended transitions often disable the baseline fitting near 1 atm. Such blended spectra can be managed by a recently developed quasi-absorbance fitting procedure<sup>14</sup> if the temperature is roughly uniform, but this procedure fails when the temperature is highly nonuniform. There is currently no simple scheme available to determine the  $a_i$  in blended spectra when nonuniform temperatures are present. However, if the broadening parameters  $2\gamma(T, P, x_j)$  are known, the problem is tractable, and not only the  $a_i$  but also the line-shape information measured can in principle be used to determine flow properties.

### C. Condition Number and Absorption Line Selection

The framework of the discretization technique provides a basis for choosing the optimum lines for a given temperature distribution measurement; line selection can be based on the condition number of the line-strength matrix  $\mathbf{S}$ . Although the line selection strategy is derived from the discretization technique, the strategy will generally optimize the performance of the distribution fitting technique as well.

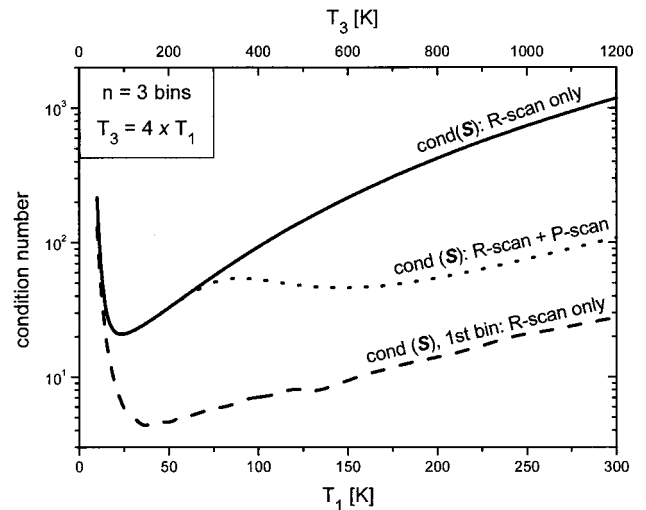


Fig. 12. Condition number of the line-strength matrix  $\mathbf{S}$  generated from the *R*-scan transitions (solid curve) and from the *R*-scan and *P*-scan transitions (dotted curve), indicating that the addition of the *P*-scan lines reduces the measurement error at high temperatures. The componentwise condition number estimate (dashed curve) demonstrates that the measurement error can be bin specific. Such information is useful for the selection of the optimum absorption lines for a given measurement.

Typically, Eq. (5) should be cast as a linear least-squares problem for  $\mathbf{x}$  when we choose  $m > n$ . The solution to Eq. (5) is then  $\mathbf{x} = \mathbf{S}^+ \mathbf{a}$ , where  $\mathbf{S}^+$  is the Moore–Penrose pseudoinverse of  $\mathbf{S}$ . The sensitivity of the solution  $\mathbf{x}$  to the uncertainties in  $\mathbf{S}$  and  $\mathbf{a}$  is characterized by the condition number of  $\mathbf{S}$ :

$$\text{cond}(\mathbf{S}) = \|\mathbf{S}\|_2 \|\mathbf{S}^+\|_2 = \sigma_{\max}(\mathbf{S}) \sigma_{\max}(\mathbf{S}^+) = \frac{\sigma_{\max}(\mathbf{S})}{\sigma_{\min}(\mathbf{S})}, \quad (6)$$

where  $\sigma_{\max}(\mathbf{S})$  and  $\sigma_{\min}(\mathbf{S})$  are the maximum and minimum singular values of  $\mathbf{S}$ . The relative error in the solution vector  $\mathbf{x}$ ,  $\|\delta\mathbf{x}\|_2 / \|\mathbf{x}\|_2$  ( $\delta\mathbf{x} \equiv \mathbf{x}_{\text{measured}} - \mathbf{x}_{\text{actual}}$ ), is bounded according to

$$\frac{\|\delta\mathbf{x}\|_2}{\|\mathbf{x}\|_2} \leq \text{cond}(\mathbf{S}) \frac{\|\delta\mathbf{a}\|_2}{\|\mathbf{a}\|_2}, \quad (7)$$

so that the maximum relative error in  $\mathbf{x}$  is simply the relative error in the measured  $\mathbf{a}$  vector, amplified by the condition number of  $\mathbf{S}$ . Hence absorption lines should be selected to minimize  $\text{cond}(\mathbf{S})$  for a given sensor application.

Figure 12 shows condition number calculations relevant to the measurements described in this paper. Using a temperature bin vector with  $n = 3$  equally spaced bins, we show  $\text{cond}(\mathbf{S})$  versus  $T_1$ , with  $T_3$  set equal to  $4 \times T_1$ , for the *R*-scan matrix  $\mathbf{S}$  (solid curve) and the *R*-scan and *P*-scan matrix  $\mathbf{S}$  (dotted curve). In addition to this standard condition number  $\text{cond}(\mathbf{S})$ , results from a statistical condition number estimate<sup>23</sup> are shown for the *R*-scan matrix  $\mathbf{S}$  (dashed curve). The statistical condition number provides the relative sensitivity of individual components of  $\mathbf{x}$

to the problem; the curve shown in Fig. 12 is for the first component of  $\mathbf{x}$ ,  $\mathbf{x}(1)$  and thus represents the sensitivity for the first temperature bin only. The componentwise and standard condition numbers differ, indicating that the elements of  $\mathbf{x}$  have different sensitivities and that a single condition number is somewhat inappropriate.

It is clear from Fig. 12 that the  $R$ -scan matrix  $\mathbf{S}$  is best suited to low temperatures for two reasons. First, all curves have minima at very low temperatures ( $T_1 \sim 30$  K; liquefaction is ignored in Fig. 12). Second, the componentwise condition number for  $\mathbf{x}(1)$  is much smaller than the standard condition number  $\text{cond}(\mathbf{S})$ . This implies that the measurement error in the low-temperature bins will be less than the error in the higher-temperature bins, which is exactly what we observed, for example, in the measurement results shown in Fig. 6.

That the  $R$ -scan matrix  $\mathbf{S}$  is conditioned for low temperatures is consistent with a result from the two-line technique<sup>21</sup>: The peak temperature sensitivity for a specific line pair occurs at

$$T = \left( \frac{hc}{2k} \right) (E_1'' - E_2'') \approx 0.72 \Delta E'' \quad (8)$$

For these ten lines (see Table 1), the maximum  $\Delta E''$  is  $304 \text{ cm}^{-1}$ , which means that each possible pair of lines made from these ten, taken independently, will have a peak sensitivity at a temperature  $\leq 0.72 \times 304 = 218$  K. When the  $P$ -scan lines are included, Eq. (8) predicts better sensor performance at higher temperatures: The maximum  $\Delta E''$  becomes  $1043 \text{ cm}^{-1}$  and therefore each pair of lines made from the 16 total lines will have a peak sensitivity at a temperature  $\leq 751$  K instead of  $\leq 218$  K. Indeed, as shown in Fig. 12,  $\mathbf{S}$  becomes relatively well conditioned at higher temperatures when the  $P$ -scan lines are included. This is why the  $P$ -scan lines were needed to achieve the results of Fig. 8.

The results of Fig. 12 correspond to  $n = 3$  bins; similar calculations show that, with each bin added, the curves shown in Fig. 12 are shifted upward approximately 1 order of magnitude. This dramatic increase confirms the expected result, namely, that one should choose the smallest number of bins allowable for a specific sensor application. Choosing a small number of bins, for example, enabled us to obtain the results of Fig. 10(a) even though we used only the  $R$ -scan lines.

The absolute value of the Fig. 12 condition numbers overestimates the absolute error realized when a NNLS solver is used to solve  $\mathbf{S}\mathbf{x} = \mathbf{a}$ ; because the NNLS solver constrains the solution, excluding negative values in the solution vector  $\mathbf{x}$ , the errors are reduced. The trends, however, remain as predicted, and the condition number remains an appropriate figure of merit to optimize sensor performance.

#### D. Simulating Sensor Performance

When either the discretization or the distribution fitting technique is used, the following steps are recom-

mended to optimize and simulate sensor performance. First, optimize the absorption line selection, guided first by Eq. (8) and then by the condition number of  $\mathbf{S}$  as described above. With the optimized matrix  $\mathbf{S}$  and an expected mole fraction vector  $\mathbf{x}_{\text{exact}}$ , calculate  $\mathbf{a}$  by use of Eq. (5); this can be called  $\mathbf{a}_{\text{exact}}$ . Generate realistic vectors  $\mathbf{a}_{\text{measured}}$  by the addition of random noise to  $\mathbf{a}_{\text{exact}}$  (1–10% peak-to-peak noise is reasonable, depending on the application), and solve for simulated vectors  $\mathbf{x}_{\text{measured}}$  by use of a NNLS or nonlinear function minimization algorithm, depending on the technique chosen. Finally, compare  $\mathbf{x}_{\text{measured}}$  to  $\mathbf{x}_{\text{exact}}$  to estimate the expected accuracy of the sensor. For all the measurements presented above, the sensor performance predicted by such simulations agreed well with the final results.

## 5. Conclusions

A simple absorption sensor for line-of-sight temperature distribution measurements, enabled by recently developed VCSEL sources, has been demonstrated in flows containing controlled nonuniformities in the 200–700 K range. The current realization of the sensor utilizes  $\text{O}_2$  A-band transitions, but future sensors of this type may be developed for other species and temperature ranges.

Widely tunable VCSELs are responsible for the relative simplicity of the sensor. Each VCSEL used in the sensor effectively replaces approximately ten multiplexed Fabry–Perot or DFB lasers; thus a traditional diode-laser sensor, retrofitted to use VCSELs, can realize a tenfold increase in the measured flow information. The increased information has been used, in this case, to provide enhanced temperature measurements along a single line of sight.

Two techniques for reducing the increased information to temperature distributions have been developed: the discretization technique and the distribution fitting technique. The discretization technique is faster because it is based on a linear system. Also, it is applicable to flows with arbitrary nonuniformities: Only the expected minimum and maximum temperatures are required to find the distribution of absorber column density versus temperature. For simple flows, the results of column density versus temperature can be reduced to more meaningful information. The distribution fitting technique is generally more accurate and robust. However, it is applicable only to flows that have temperature and absorber mole fraction distributions that can be accurately modeled by a general functional form. Although the discretization technique is well suited to arbitrary flows and the distribution fitting technique is most appropriate for well-understood flows, the best technique depends strongly on the details of the specific sensor application.

Line selection based on the condition number has been shown to be useful to optimize sensor performance for a given species and temperature range. Both data reduction techniques can be optimized

with the same line selection strategy. The accuracy of either technique always increases with the number of absorption lines probed, but increases most dramatically with the addition of lines having properly chosen lower-state energies.

The sensing strategy has been demonstrated for two atmospheric-pressure test cases with controlled nonuniformities: a two-temperature path and a path containing a linear temperature distribution. The successful results obtained in the sensor demonstration experiments encourage application of the sensor to industrial flows in which temperature distributions are of interest. Because of its simplicity and the expanded data it provides, the sensor is expected to enable novel flow monitoring and control schemes.

This research was supported by the U.S. Office of Naval Research, with Gabriel Roy as the technical monitor, and the U.S. Air Force Office of Scientific Research, Aerospace Sciences Directorate, with Julian Tishkoff as the technical monitor.

## References

1. X. Ouyang and P. L. Varghese, "Line-of-sight absorption measurements of high temperature gases with thermal and concentration boundary layers," *Appl. Opt.* **28**, 3979–3984 (1989).
2. S. M. Schoenung and R. K. Hanson, "CO and temperature-measurements in a flat flame by laser-absorption spectroscopy and probe techniques," *Combust. Sci. Technol.* **24**, 227–237 (1981).
3. E. R. Furlong, "Diode-laser absorption spectroscopy applied for the active control of combustion," Ph.D. dissertation, Thermosciences Division Report 116 (Mechanical Engineering Department, Stanford University, Stanford, Calif., 1998).
4. E. R. Furlong, R. M. Mihalcea, M. E. Webber, D. S. Baer, and R. K. Hanson, "Diode-laser sensors for real-time control of pulsed combustion systems," *AIAA J.* **37**, 732–737 (1999).
5. J. Wang, M. Maiorov, J. B. Jeffries, D. Z. Garbuzov, J. C. Connolly, and R. K. Hanson, "A potential remote sensor of CO in vehicle exhausts using 2.3  $\mu\text{m}$  diode lasers," *Meas. Sci. Technol.* **11**, 1576–1584 (2000).
6. J. M. Seitzman, R. Tamma, and B. Scully, "Broadband infrared sensor for active control of high pressure combustors," paper AIAA-98-0401, presented at the Thirty-Sixth Aerospace Sciences Meeting and Exhibit, Reno, Nev., 12–15 Jan. 1998 (American Institute of Aeronautics and Astronautics, New York, 1998).
7. L. R. Brown and C. Plymate, "Experimental line parameters of the oxygen A band at 760 nm," *J. Mol. Spectrosc.* **199**, 166–179 (2000).
8. K. J. Ritter and T. D. Wilkerson, "High-resolution spectroscopy of the oxygen A band," *J. Mol. Spectrosc.* **121**, 1–19 (1987).
9. L. S. Rothman, C. P. Rinsland, A. Goldman, S. T. Massie, D. P. Edwards, J.-M. Flaud, A. Perrin, C. Camy-Peyret, V. Dana, J.-Y. Mandin, J. Schroeder, A. McCann, R. R. Gamache, R. B. Wattson, K. Yoshino, K. V. Chance, K. W. Jucks, L. R. Brown, V. Nemtchinov, and P. Varanasi, "The HITRAN molecular spectroscopic database and HAWKS (HITRAN ATMOSPHERIC WORKSTATION): 1996 edition," *J. Quant. Spectrosc. Radiat. Transfer* **60**, 665–710 (1998).
10. L. C. Philippe and R. K. Hanson, "Laser-diode wavelength-modulation spectroscopy for simultaneous measurement of temperature, pressure, and velocity in shock-heated oxygen flows," *Appl. Opt.* **32**, 6090–6103 (1993).
11. R. Benedetti, K. Giulietti, and M. Rosa-Clot, "Line shape analysis of  $\text{O}_2$  in air as a way to measure temperature using a DFB-diode-laser at 761 nm," *Opt. Commun.* **154**, 47–53 (1998).
12. T. Drier and G. Schiff, "High temperature  $\text{O}_2$ -CARS thermometry," *Appl. Phys. B* **55**, 388–390 (1992).
13. P. Macko and P. Veis, "Time resolved  $\text{O}_2(\text{b}^1\Sigma_g^+)$  rotational temperature measurements in a low-pressure oxygen pulsed discharge. Simple and quick method for temperature determination," *J. Phys. D* **32**, 246–250 (1999).
14. J. Wang, S. T. Sanders, J. B. Jeffries, and R. K. Hanson, "Oxygen measurements at high pressures using vertical cavity surface-emitting lasers," *Appl. Phys. B* **72**, 865–872 (2001).
15. H. P. Zappe, M. Hess, M. Moser, R. Hovel, K. Gulden, H. Gauggel, and F. Monti di Sopra, "Narrow-linewidth vertical-cavity surface-emitting lasers for oxygen detection," *Appl. Opt.* **39**, 2475–2479 (2000).
16. J. A. Silver and D. J. Kane, "Diode laser measurements of concentration and temperature in microgravity combustion," *Meas. Sci. Technol.* **10**, 845–852 (1999).
17. H. Braun, A. Hoeren, T. Schneiders, K. Vortmeyer, and H. Pfost, "Measurement of the mixing quality in premix combustors," *Energy Convers. Manage.* **39**, 1991–1999 (1998).
18. S. F. Frey, A. R. Eaton, D. M. Cusano, M. W. Plesniak, and P. E. Sojka, "Effect of inlet turbulence and premixer length on fuel distribution in swirling gas-turbine premixer," *J. Propul. Power* **16**, 837–844 (2000).
19. M. P. Arroyo, S. Langlois, and R. K. Hanson, "Diode-laser absorption technique for simultaneous measurements of multiple gasdynamic parameters in high-speed flows containing water vapor," *Appl. Opt.* **33**, 3296–3307 (1994).
20. D. S. Baer, R. K. Hanson, M. E. Newfield, and N. Gopaul, "Multiplexed diode-laser sensor system for simultaneous  $\text{H}_2\text{O}$ ,  $\text{O}_2$ , and temperature measurements," *Opt. Lett.* **19**, 1900–1902 (1994).
21. M. P. Arroyo and R. K. Hanson, "Absorption-measurements of water-vapor concentration, temperature, and line-shape parameters using a tunable InGaAsP diode laser," *Appl. Opt.* **32**, 6104–6116 (1993).
22. J. A. Silver, D. J. Kane, and P. S. Greenberg, "Quantitative species measurements in microgravity flames with near-IR diode-lasers," *Appl. Opt.* **34**, 2787–2801 (1995).
23. C. S. Kenney, A. J. Laub, and M. S. Reese, "Statistical condition estimation for linear least squares," *SIAM J. Matrix Anal. Appl.* **19**, 906–923 (1998).